Induced circular dichroism from helicoidal nano substrates to porphyrins: The role of chiral self-assembly

Gautier Duroux, Lucas Robin, Peizhao Liu, Emilie Dols, Lima Mendes Matheus De Souza, Sonia Buffiere, Elodie Pardieu, Antoine Scalabre, Thierry Buffeteau, Sylvain Nlate, et al.

Induced circular dichroism from helicoidal nano substrates to porphyrins: The role of chiral self-assembly

Gautier Duroux,[a] Lucas Robin,[b] Peizhao Liu,[a] Emilie Dols,[a] Matheus De Souza Lima Mendes,[a] Sonia Buffière,[b] Elodie Pardieu,[b] Antoine Scalabre,[a] Thierry Buffeteau,[c] Sylvain Nlate,[a] Reiko Oda,[a] Maria Sara Raju,[d] Matteo Atzori,[d] Cyrille Train,[d] Geert L. J. A. Rikken,[d] Patrick Rosa,[b] Elizabeth A. Hillard,*[b] Emilie Pouget*[a]

Because the combination of chiral and magnetic properties is becoming more and more attractive for magneto-chiral phenomena, we here aim at exploring the induction of chirality to achiral magnetic molecules as a strategy for the preparation of magneto-chiral objects. To this end, we have associated free base- and metallo-porphyrins with silica nano helices, using a variety of elaboration methods and studied them mainly by electronic natural circular dichroism (NCD) and magnetic circular dichroism (MCD) spectroscopies. While electrostatic or covalent surface grafting uniformly yielded very low induced CD (ICD) for the four assayed porphyrins, a moderate response was observed when the porphyrins were incorporated into the interior of the double-walled helices, likely due to the association of the molecules with the chirally-organized gemini surfactant in the helices' interior. A generally stronger, but more variable, ICD was observed when the molecules were drop casted onto the helices immobilised on a quartz plate, likely due to the different capacities of the porphyrins to aggregate into chiral assemblies. Electronic spectroscopy, electron microscopy and IR spectroscopy were used to interpret the patterns of aggregation and their influence on ICD and MCD. No enhancement of MCD was observed as a result of association with the nanohelices except in the case of the free base, 5,10,15,20-tetra-(4-sulfonatophenyl)porphyrin (TPPS). This nanocomposite demonstrated a large ICD in the Soret region and a large MCD in the Q-region due to J-aggregation. However, no induced MChD was observed, possibly due to the spectral mismatch between the ICD and MCD peaks.

Introduction

Induced circular dichroism (ICD), which refers to the observation of natural optical activity in achiral objects through their interaction with chiral ones, was initially demonstrated in 1966[1] and theoretically described in 1975.[2] Two principal mechanisms for ICD have been proposed.[3] The first is based on the interaction of the chiral object with the achiral molecule, where the former breaks the mirror symmetry of the latter. The second mechanism does not imply any structural change in the achiral molecule, but its electric transition moments become coupled within a chiral assembly. ICD has been detected in a number of molecular systems, including the influence of chiral solvents on achiral solutes[1] and the interactions between chiral hosts and achiral guests.[4,5] More recent studies confirm the importance of ICD in creating enantioselective catalysts based on copper embedded in supramolecular helices,[6] chiral luminescent systems from non-chiral luminophores included in chiral assemblies of glutamic acid derivatives,[7] chiral photonic assemblies of gold nanoparticles with peptides[8] or DNA[9], and sensors based on chiral amplification.[10]

One potential use of ICD is in the field of Magneto-Chiral Dichroism (MChD), an optical effect where the absorption coefficient of a chiral system changes based on its handedness when irradiated by unpolarized light in the presence of an external magnetic field along the direction of the light propagation wave vector.[11–19] Baranova *et al.*, proposed a theory of MChD which states that it is directly proportional to the product of the natural circular dichroism (NCD) and magnetic circular dichroism (MCD) response of the material.[20] Although NCD and MCD effects are phenomenologically similar, their origins, being molecular chirality and the magnetic dipole moment of the molecule, respectively, are different though ultimately related to the influence of these two characteristics on the electronic structure. It has been predicted that MChD effects should be the strongest when the chiral and magnetic center is the same,[21] but recent studies reveal that in some cases, electronic transitions that only have strong natural or magnetic optical activity can lead to the observation of MChD.[22]

The motivation behind this study is therefore to explore the mechanism of interplay between ICD and MCD and evaluate the parameters necessary to generate an induced MChD response. We focus the present work on porphyrins, conjugated pyrrole-based heterocycles with strong absorption in the visible region. Porphyrins typically have Soret bands between 380 and 500 nm (representing the $S_0 \rightarrow S_2$ transition) and less intense Q-bands between 500 and 750 nm ($S_0 \rightarrow S_1$).[23] Due to their planar nature, porphyrins easily form different types of assemblies. The most common types are H-aggregates and J-aggregates. H-aggregates are characterized by a co-facial stacking of the porphyrins, resulting in a blue shift in the Soret band with a typical spectral shift from nm to few tens of nm.[24] On the other hand, J-aggregates have a staircase-like structure, giving rise to a sharp, intense red-shifted Soret band, also known as the "J-peak".[25] The red-shift is quite significant, being almost 40 nm between the free-base and the J-aggregate of tetraphenylprophyrin.[26] J-aggregates also evince a red-shift in the Q-band(s), which depends on the aromatic substitution, being almost 80 nm for tetraphenylprophyrin.[26] J-aggregation can result in an orientation of the transition dipoles,[26] an arrangement which is particularly favorable for ICD.[24] The magnetic moment in porphyrins arises from the circulation of π-electrons in the conjugated system,[27] as well the magnetic moment of the metal (if present), and aggregation can also give rise to

peaks in the Soret[27] and Q-band regions of the MCD spectra.[28] For this reason, such assemblies have the potential to exhibit significant ICD and MCD, making them promising candidates for showing induced MChD signals.[13,29] Recent research by Ishii and coworkers has shown interesting results in this direction.[27]

We have been investigating ICD phenomena using silica nanohelices, obtained by the mineralization of a helical nanotemplate made from the 16-2-16 gemini surfactant associated with chiral tartrate counter ions.[30–33] The nanohelices are described as "hybrid" when the interior organic template is kept intact or "inorganic" when the organic template is removed by washing the material with methanol (Figure 1A).[34,35] Using this system, we have reported ICD for various substances such as chromophores,[35] catalysts,[36,37] halide anions,[38] and nanoparticles[39,40] associated with the helices with different methods (Figure 1B). The first approach involves grafting molecular chromophores or nanoparticles electrostatically or covalently on the inorganic silica surface modified with amine groups (Figure 1B1). [36,39,41] In the second method, using hybrid helices, the tartrate anions confined in the helical nanospace inside the silica nano helices were replaced by non-chiral anions (Figure 1B3). This approach will be referred to as "ion exchange" (IEx) hereafter.[35,38] The gemini surfactants, confined inside the nanospace of the silica nanohelix, maintain their chiral and crystalline conformation[42] even after the removal of tartrate, and are capable of transmitting the chiral information to the achiral anions which replace tartrate.[43–45] Notably, we have recently demonstrated ICD on 5,10,15,20-tetra-(4-sulfonatophenyl)porphyrin (**TPPS**) by IEx using the hybrid nanohelices.[43]

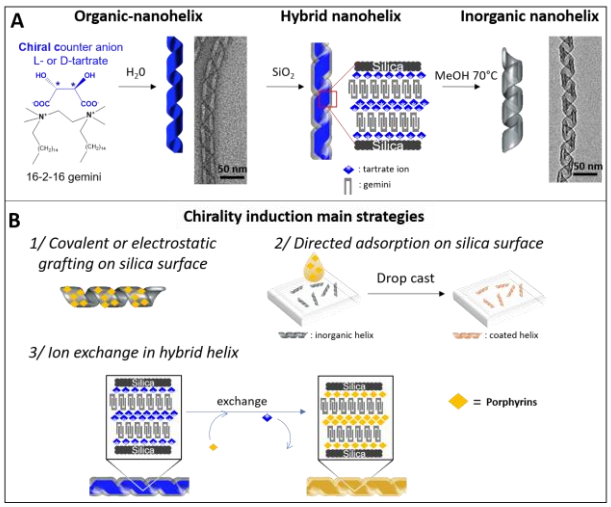

Figure 1. A) Synthetic pathway of the organic, hybrid and pure silica nanohelices. B) Main strategies used for chirality induction on porphyrins: 1) direct grafting, 2) surface adsorption directed on the silica nanohelices by drop casting and 3) ion exchange of the gemini counter ion inside the silica wall of the hybrid helices.

Finally, more recently, we have investigated the association of metal salts with the helices using sequential drop casting (DC) of the helices and the chromophore solution onto a quartz plate (Figure 1B2). These ions in contact with the helices on the substrate concentrate themselves inside the helical nano-space of the silica *via* capillary forces as they dry, giving rise to helical shaped crystal growth, leading to strong ICD and Induced Circularly Polarized Luminescence (ICPL).[46]

Here we report ICD and MCD investigations of nanocomposites fabricated using different chiral induction strategies on free base **TPPS**, iron(III)- and copper(II)-TPPS (**Fe-Cl-TPPS** and **Cu-TPPS**, respectively) and the naturally-occurring iron(III) porphyrin, **hemin** (Chart 1). We observed that the diverse patterns of porphyrin self-assembly which are associated with different molecular geometries and functional groups result in variable spectroscopic responses. Such observations provide insight into the importance of the self-assembly mechanisms in induced chiroptical and magnetoptical properties.

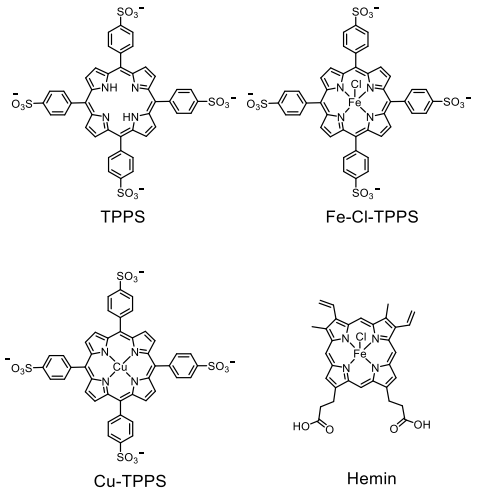

Chart 1.

Results

Figure 1B illustrates three methods for associating the nanohelices with the porphyrins shown in Chart 1: direct surface grafting (electrostatic or covalent), IEx using hybrid helices, and DC using inorganic helices.

To perform surface grafting, the silica surfaces were functionalized with aminosilane, resulting in a positively charged surface. This allowed the carboxylate (**hemin**) or sulfonate groups (**TPPS, Fe-Cl-TPPS**, **Cu-TPPS**) to associate with the surface through electrostatic interactions. The carboxylate group of **hemin** was also activated using 1-ethyl-3-[3-(dimethylamino)propyl]carbodiimide and hydroxybenzotriazole (HOBT) in order to form a peptidic bond with the aminated silica.[47] After removal of excess porphyrin, the helices were imaged using Transmission Electron Microscopy (TEM). While the contrast of the helices on the TEM images as well as the UV-vis absorption spectra (Figure

SI-1a) showed the presence of grafted molecules on the surface of the helices, only very weak ICD was observed. Using the differential molar extinction coefficient of left and right circularly polarized light, denoted as $\Delta\varepsilon$, we determined the dimensionless anisotropic ratio $g = \Delta A/A = \Delta\varepsilon/\varepsilon$ (see detailed definition in SI-2) as presented in Figure 2, revealing low *g*-factors (around 10^{-4}) for the direct grafting process.

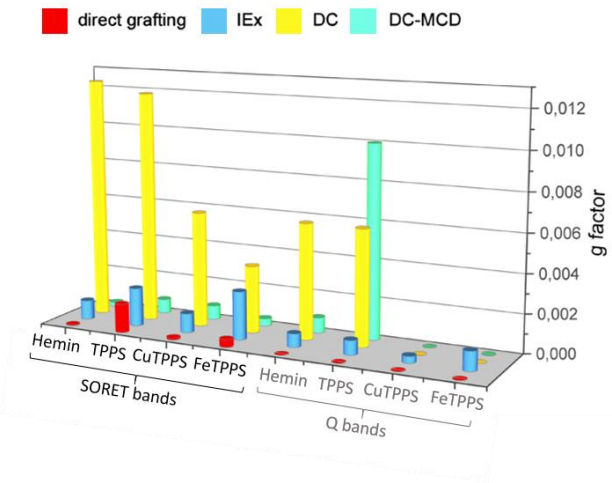

Figure 2. Maximum ICD g-factors on the Soret and Q bands for all the studied samples (nature of the porphyrins and nature of the interaction with the nanohelices) and MCD g-factors for the DC samples.

In order to obtain IEx systems, hybrid helices were used where the tartrate anion was replaced by a chloride anion, as previously described.[38] The helices were incubated in an aqueous solution of porphyrin at 4° C overnight, and washed with water to remove excess porphyrin. The TEM images, shown in Figure 3A, reveal that the helicity is retained even after treatment with the chromophores. Compared to the naked helix shown in Figure 1, slightly higher contrast of the images suggests the presence of the porphyrins, which is also confirmed by absorption spectra (Figure 3B). The CD spectra of the IEx samples (Figure 3B) deposited on quartz plates are compared to the samples prepared by the DC method. These CD spectra qualitatively show mirror image responses in the presence of nanohelices with opposite helicities (right vs left). For all the samples, an increase of the signal is observed below 300 nm, corresponding to the chiral scattering of light by the silica helices in the solid state.[48] Notably, for all of the porphyrins, opposite Soret band signals are observed around 425-440 nm, with a negative value for the left-handed helices and a positive one for the right-handed helices. Less intense, but nonetheless unambiguous ICD is also observed in the Q-bands (between 500 and 700 nm), with the same sign as the Soret bands.

The DC method was optimized by maximizing the ICD signal as a function of solvent, helix-molecule ratio, and evaporation temperature using **hemin** (details in SI-3). The evolution of the *g* factors shows that the optimal process corresponds to 100 µg of

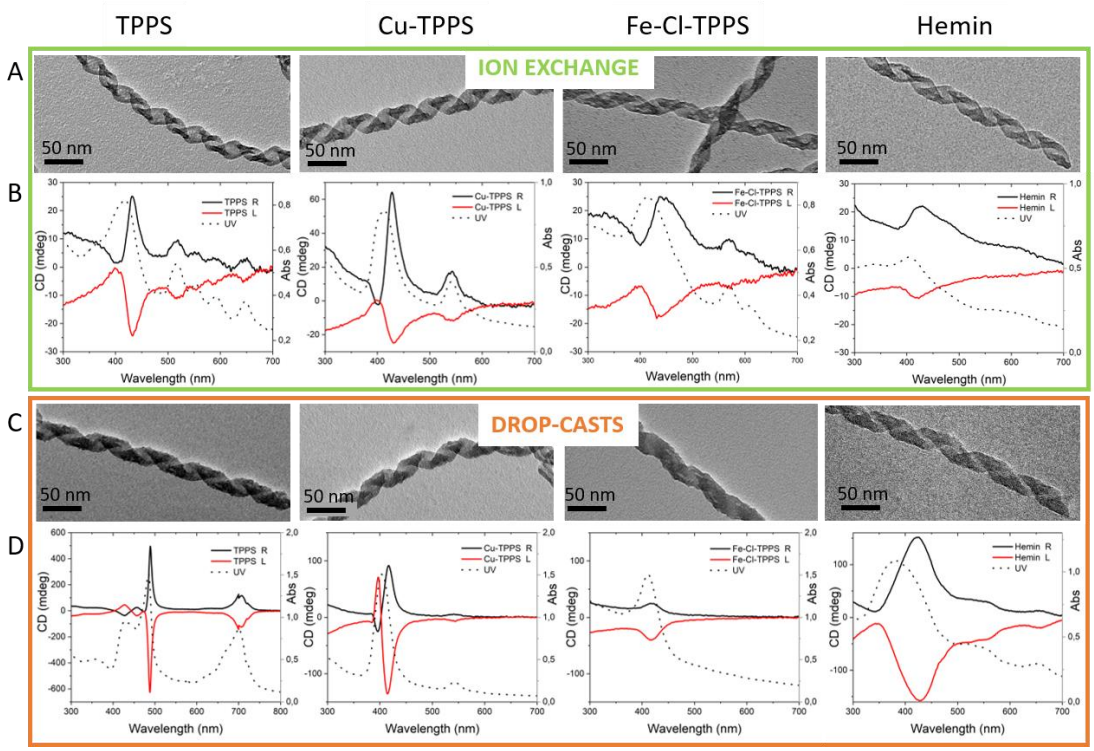

Figure 3. TEM images and their corresponding CD spectra (solid lines) and absorption spectra (dashed lines) for all the nanocomposites, for the chiral induction strategies of ion exchange (top) and drop casting (bottom). Note that the wavelength scale in the TPPS DC spectra is different than the others.

silica nanohelices first deposited via drop-casting on a quartz plate of 1 cm, followed by drop-casting 7.5 µL of a 5 mM solution of porphyrin in DMF at 20°C. As observed in the TEM images (Figure 3C), for which the preparation is detailed in the experimental section, the darker and thicker silica helices, indicate the presence of a layer of molecules deposited on the silica walls compared to the bare silica (Figure 1A) and hybrid helices (Figure 3A). In order to evaluate the concentration and visualize the distribution of the porphyrins on the sample plates after the application of the three methods, Energy Dispersive Spectroscopy (EDS) measurements were performed using **hemin** as a model compound. The atomic concentration of iron with respect to silicon increased from 3 at% for the covalent grafting to 5 at% for the IEx sample to 10 at% for the DC sample. The element mapping carried out during these experiments confirmed that, for the DC sample, the iron is specifically deposited on or inside the silica wall and not randomly spread on the TEM grid surface (Figure 4).

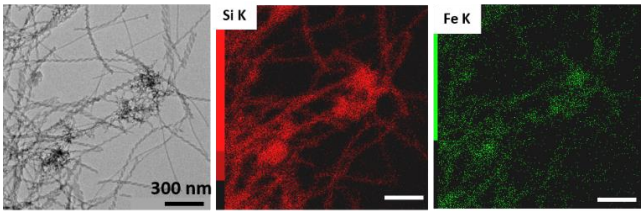

Figure 4. EDS mapping of the drop casted hemin on the silica helices. Elemental analysis of Si and Fe shows the good repartition of the Fe on the surface of the silica. The quantification gives an atomic ratio Fe/Si of 10 at% (the same quantifications give ratios of 5 at% and 3 at% for the IEx and covalent grafting samples respectively).

The CD signals obtained for the DC samples (Figure 3D) are quite variable, being higher than the IEx technique for all of the compounds except **Fe-Cl-TPPS**. Notably, the DC free base **TPPS** yielded a very thin and intense band at 490 nm with excitonic coupling indicative of aggregation and characterized by the right-handed helices giving a negative band and two positive ones, and vice versa for the left-handed helices. The *g*-factor of this band is higher than 10^{-2} (Figure 2), indicative of a well-organized and coupled assembly.[29,49,50] A similarly large *g*-factor is observed for the Soret band of DC **hemin**, but it is much broader and lacks excitonic coupling. DC **Cu-TPPS** and DC **Fe-Cl-TPPS**, also present ICD on the Soret bands with lower *g*-factor values around 10^{-3}. The ICD of **Cu-TPPS** is more pronounced than **Fe-Cl-TPPS**, and presents excitonic coupling, where **Fe-Cl-TPPS** does not. Regarding the Q-bands, DC **TPPS** exhibits ICD at around 700 nm which shows a broad band with up to two shoulders, unlike the IEx samples that have four discrete bands of much lower intensity. Globally, the metal TPPS compounds show low ICD intensity on the Q-bands, becoming imperceptible for **Fe-Cl-TPPS**.

MCD spectra were measured under a magnetic field of ±1.6 T at room temperature for the porphyrins in solution (Figure SI-4) and the DC samples (Figure SI-5). Regarding the MCD of the isolated porphyrins in solution, the *g* values in both the Soret and Q band region are on the order of 10^{-3}, except in the case of hemin, where the MCD of the Soret band is vanishingly small. For the DC samples with helices, the data presented in Figure SI-5 corresponds to the CD measurements under the external magnetic field, from which we subtracted the CD data under $B = 0$, giving the purely magnetic response of the samples. The hemin sample shows two small peaks in the Q-band region, with a *g* factor of the order of 10^{-4}, while **Cu-TPPS** and **Fe-Cl-TPPS** show MCD only on the Soret band (see all the MCD g-factors in green in the graph Figure 2). Interestingly, the MCD signal in the Q-band region for free base **TPPS** is exalted for the DC samples, with a g-factor reaching 10^{-2}. Meanwhile, the MCD bands in the Soret region are an order of magnitude smaller. Finally, none of these systems show observable MChD signals in spite of the strong ICD and MCD, particularly for the free **TPPS** DC system.

Discussion

The results presented above show that the silica nanohelices can induce a chiroptical response from a variety of achiral porphyrins. The ICD signals vary considerably depending the sample preparation conditions. Compared to the direct grafting of the molecules to the silica surface by electrostatic or covalent interactions which showed relatively weak ICD signals with low *g*-factors, both the IEx in the hybrid nanohelices and the DC methods yielded much higher ICD signals. The results also varied depending on the nature of the porphyrin. While all of the porphyrins gave similar ICD intensities using the grafting or IEx method, the response varied significantly depending on the nature of the porphyrin using the DC method. This suggests that the compounds are likely organized similarly in the composites formed by way of grafting or IEx, but are differently organized in the DC nanocomposites. This also holds for the MCD signals, which varied significantly depending on the porphyrin using the DC method, being extremely weak in the metallo-porphyrins, but remarkably strong in the Q-band region of free base **TPPS**.

As previously mentioned, UV-vis spectroscopy can be used to detect and identify porphyrin aggregates. For the covalent and electrostatically grafted samples, no aggregation, J or H, is observed, with red- or blue-shifted peaks respectively. Indeed, the UV/vis spectra of the nanocomposites resemble the spectra of the molecules in solution (Figure SI-1a). In the case of IEx (as shown in Figure 5), the bands for **TPPS** and **Cu-TPPS** appear in the same energy ranges as found in solution, suggesting a lack of aggregation between the porphyrin molecules. For **Fe-Cl-TPPS** and **hemin**, a small red-shift in the Soret band is observed. In **Fe-Cl-TPPS**, the

Soret band in water shows a main feature at 390 nm (monomer) and a shoulder at 420 nm which has been attributed to a μ-oxo dimer.[51] For the IEx sample, the band associated with the dimer becomes the primary one, with only a negligible shoulder at 475 nm, suggesting only a slight increase in the interactions between the molecules when associated with the helices. A similar behavior is observed for **hemin**. These results suggest that for the IEx samples, the porphyrins exist in the helices in a non-aggregated state, being dimers at most. However, we nonetheless see a significant ICD for the molecules, suggesting a close interaction of the molecule with the chirally-organized gemini giving rise to chirality induction.

Regarding the porphyrins interacting with the helices in the DC samples, the results are quite variable, depending on the porphyrin (Figure 5). The Soret bands of the DC **TPPS** are clearly red-shifted to 485 nm compared to the molecular solution, while the Q-bands coalesce into a broad band at 700 nm, both phenomena suggesting the formation of J-aggregates.[24,52] As already observed by Ishii and co-workers,[13] J-aggregation appears to be of utmost importance in chirality induction of porphyrins and the observed excitonic coupling. Indeed, **TPPS** J-aggregates have been widely studied, and arise from the interaction of the negatively charged sulfonate group with the protonated pyrrole core at pH < 4.8.[52] On the contrary, for **Cu-TPPS** in DC helices, no red-shift is observed, consistent with previous studies that show that **Cu-TPPS** does not form J-aggregates, probably because the aggregation is blocked by the Cu(II) center.[52,53] Instead, a small blue shift of the Soret band is observed, indicating the formation of H-aggregates. For **Fe-Cl-TPPS** and **hemin**, the position of the main Soret band in the DC spectra are quite similar to those from the IEx method, again suggesting that the aggregation is likely limited to dimerization. Indeed, the presence of the axial chloride ligand would be expected to limit J-aggregation. However, the ICD response of **hemin** is nonetheless substantial, suggesting the presence of a different kind of organization.

To study the organization of **hemin**, infrared (IR) spectroscopy was used. For the IEx sample, no band is observed between 1700-1750 cm^{-1}, the spectral range characteristic to the νC=O mode of COOH groups, indicating that all the hemin carboxylato groups are deprotonated and likely associated with the positively charged gemini surfactants. This interpretation is supported by the fact that the ν_aCOO^- and ν_sCOO^- bands appear at 1563 and 1399 cm^{-1}, respectively, as shown in Figure 6A. The presence of these two bands indicates an electrostatic interaction between the carboxylate groups and the quaternary ammoniums of the gemini. This kind of association with the chiral gemini is likely responsible for the moderate ICD observed, and similar associations can be envisioned for the **TPPS**-based molecules as well. Unfortunately,

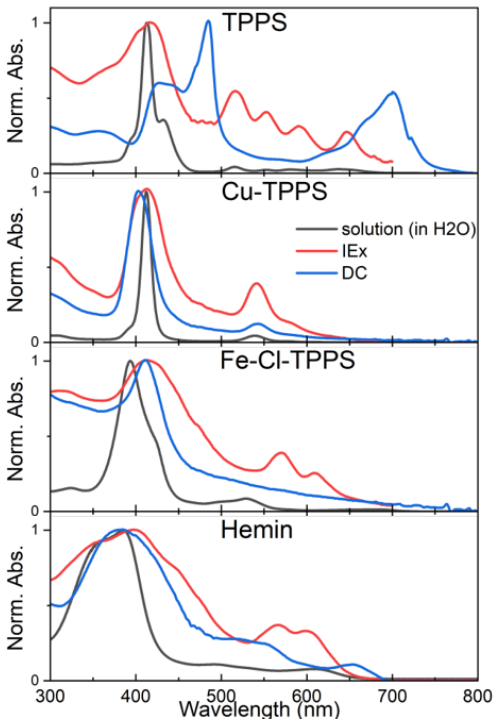

Figure 5. Normalized UV/vis spectra comparisons of the different porphyrins in solution, in the hybrid samples (IEx) and in the drop casted samples. Path length of 2mm. Concentration of 0.035 mM, 0.025 mM and 0,060 mM respectively for TPPS, Cu-TPPS and Fe-Cl-TPPS solutions and of 0,150 mM for the hemin solution.

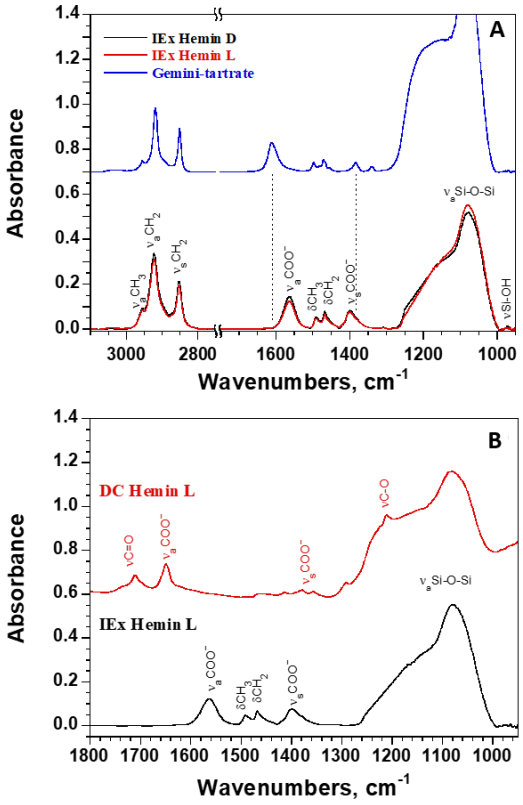

Figure 6. A) IR spectra of hybrid nanohelices (gemini-tartrate assemblage) and hemin complex in the ion exchange samples. B) Comparison of IR spectra of hemin complex prepared with the IEx and drop casting methods.

the Si-O-Si asymmetric stretching band (ν_aSi-O-Si) of the silica nanohelices results in an intense and broad band between 1000 and 1250 cm^{-1}, obscuring the response of the sulfonate group, which appears in the same spectral range.[54] Thus, only the carboxylato groups of hemin could be investigated (Figure 6).

For the DC samples of **hemin**, we observed bands related both to the acid form (1734 and 1711 cm^{-1}) and to the carboxylate form (1650 and 1379 cm^{-1}). The 1734 cm^{-1} band corresponds to the vC=O mode of "free" COOH groups whereas the 1711 cm^{-1} band is associated with the carbonyl mode of hydrogen bonded COOH groups. The 1650 and 1379 cm^{-1} bands are related to the $\nu_a COO^-$ and $\nu_s COO^-$ modes, respectively, of the carboxylate form of **hemin**, which is certainly due to the interaction of the COO^- groups of an **hemin** molecule with the iron atom of a neighboring molecule. This form of aggregation likely explains the much higher ICD in **hemin**, when compared to **Fe-Cl-TPPS**.

Based on all these data, we believe that the chirality induction using IEx and DC methods has different origins. In general, the ICD increases in the following manner: grafting < IEx < DC. This suggests that the more freedom the molecules have to self-organize, the higher the ensuing ICD. In the most favorable cases, it appears that the DC **TPPS** forms a J-aggregate that grows parallel to the helix, giving rise to a chiral supramolecular structure. In this case, grafting of the porphyrins to the silica surface would be expected to impede such aggregation, resulting in very limited ICD. We tested this hypothesis by drop-casting a solution of **TPPS** onto helices previously grafted with **TPPS** (CD spectra in SI-1c). Here the ICD was 10 times weaker than when **TPPS** was drop casted onto naked helices (*g*-factor is 1.3 10^{-3} vs 1.2 10^{-2}). This suggests that the grafted **TPPS** indeed hinders the growth of J-aggregates close to the silica surface. Having a molecular layer of non-J-aggregated **TPPS** separating the drop-casted TPPS and the chiral silica substrate seems to perturbate the chirality transfer. Thus, a surface free of any bonded and structurally locked molecules seems to be a better choice for chirality induction onto molecular aggregates. Likewise, the electrostatic association of the COO^- and SO_3^- groups with the N^+ head groups of the gemini restrict the molecules from efficiently aggregating in the case of the IEx, resulting in limited ICD from interaction with the chiral gemini. On the other hand, in the case of DC, the molecules are free to interact with each other during the drying directed aggregation, thus allowing the J-aggregation observed in **TPPS** which is primordial for high CD induction.

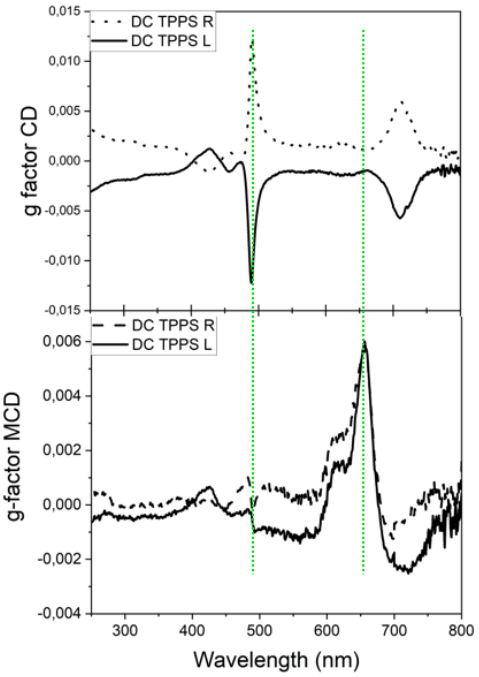

Figure 7. Comparison CD/MCD of DC TPPS. MCD is done under 1 T in the north-south direction field.

From the EDS analysis, we observed that the concentration of molecules which interact with the chiral template is a key factor to obtain stronger ICD responses. As demonstrated above, for **hemin**, the highest concentration of the molecule on the silica surface resulted in the best ICD. This again suggests that stronger interactions between the porphyrins are crucial for a strong ICD response. While we cannot unequivocally state that **TPPS** is present in higher quantities in the DC samples, EDS not being suitable for the quantification of organic molecules, we surmise that correlation of concentration with ICD intensity observed with **hemin** also holds true for **TPPS**. This interpretation is supported by the UV/vis spectra, where the absorbance of both **TPPS** and **hemin** increases in the following order: grafting < IEx < DC, which correlates with the observed ICD intensity as well.

Following the Baranova theory, the magnitude of the MChD signal can be roughly estimated as a product of g_{MCD} and g_{ICD}.[20,27] If we focus on the particularly interesting case of the **TPPS** DC nanocomposites, we observe that the material shows a very high ICD at 485 nm (Soret band) but much weaker ICD at 700 nm (Q band) whereas it shows a high MCD at 665 nm (Q band) but weak MCD at 400 nm (Soret band) (Figure 7). Due to the energy mismatch of the different absorption bands which are sensitive to either NCD or MCD, MChD is expected to be lower than the detection limits of our MChD spectrometer (10^{-4}) with a magnetic field of ± 2 T (SI-6). A similar negative result was observed on inorganic macroscopic magneto-chiroptical metasurfaces made on spiral nickel/silver nanoobjects.[55]

These results are in contrast with the previous report of Ishii and collaborators who observed MChD in the Soret band for a chiral aggregation of TPPS. This can be explained by the extremely strong ICD observed in their system, 2000 mdeg compared to the 500 mdeg in our case. Furthermore, they observed a non-negligible MCD response at the Soret band.

In the case of the metallo-porphyrins, we believe that the low aggregation state due to the presence of the metal is the origin of the lack of chirality induction preventing any possibility of creating an interesting MChD active sample. It thus appears that in the present case, ICD and MCD are mutually exclusive. In contrast with the recently studied 3d-4f chiral clusters,[20] these hybrid systems appear to essentially follow the Baranova theory.

Conclusions

We have reported the ICD and MCD of four achiral porphyrins associated to a nanometric helical silica platform. Three strategies of associating the nanohelices with the porphyrins were assayed: direct surface grafting, IEx using hybrid helices, and DC on inorganic helices. The results clearly show that the silica helices can efficiently induce CD signals to all the studied porphyrin compounds. Nonetheless, depending on the interaction between the helices and the molecules, and on the nature of the porphyrin, the ICD varies considerably. The formation of J-aggregates has been shown to play a key role and the DC technique which allowed the best head-to-tail stacking of the porphyrin led to the highest CD signals. For this reason, the highest ICD and MCD were observed with the free base porphyrin in the DC system. However, these strong ICD and MCD signals were not observed for the same transitions, Soret band for ICD and Q-band for MCD. Such an energy mismatch between the NCD- and MCD-active absorption bands are likely the origin of the absence of observable MChD signals. On the other hand, the metallo-porphyrins generally show lower ICD and MCD. We believe that the low aggregation state and the more rigid structure of the porphyrins due to the presence of the metal is at the origin of the lower efficiency on the chirality induction. It is therefore crucial to use chromophores capable of chiral aggregation showing both strong induced natural circular dichroism and magnetic circular dichroism, associated to the same electronic transition.

Experimental

Synthetic procedures

Organic nanohelices.[30,32] Enantiopure gemini-tartrate (3.58 mg, 5.10^{-3} mmol) was placed in a 15 mL Falcon centrifugation tube. Ultrapure water (5 mL) was added and the tube was left for 15 minutes in a 70°C water bath. The suspension was then stirred using a vortex and sonicated for 2 minutes. The tube was placed again in the 70°C water bath for 2 minutes, and then on a roller-mixer at 20°C for 15 minutes to cool. Finally, the mixture obtained was left to rest at 20°C for 4 days in order to let the gel self-assemble into an helicoidal shape.

Hybrid nanohelices.[32,34] Tetraethyl orthosilicate (TEOS, 250 µL, 1.1 mmol) was added to 5 mL of a 10^{-4} M enantiopure tartrate aqueous solution. The chirality of the tartrate used was the same as the chirality of the tartrate used in the synthesis of the organic nanohelices described above. The mixture was placed on a roller-mixer for 7 h at 20°C. The pre-hydrolyzed TEOS was then gently poured into the tube containing the organic nanohelices, this tube was then gently turned upside down and placed on the roller-mixer at 20°C overnight. The excess TEOS was then removed by three successive centrifugations (5 min, 3893 g, 4°C) and washing with cold (2° C) ultrapure water. One has to take care not to exceed twice the volume of the organic gel during the washings in order to stay below the critical micellar concentration (CMC).

Inorganic nanohelices.[32,34] To remove the organic surfactant inside of the silica shell, the hybrid nanohelices were washed with methanol by successive centrifugation, 5 min incubation in 60°C water bath and 5 minutes sonication. This process was repeated five times. Then the helices were washed three times with a 1:1 ethanol:isopropanol solution and were ultrasonicated with a tip-sonication processor (Vibracell 75186) in order to disentangle the helices and to cut them in tinier units (parameters are: 2mm microtip, 130W, 20kHz, 15 min with pulses of 1 s).

Ion exchange reaction.[38,43] Hybrid nanohelices (2 mg) were washed five times with a 100 mM aqueous solution of KCl at 4°C, to replace the tartrate counter-anion with chloride. After the last washing, the supernatant was decanted and replaced by a 1 mM aqueous solution of porphyrin (2 mL). The helices were resuspended using a vortex. The tube was kept at 2° C overnight for a complete ion exchange inside of the helices. The excess porphyrin was eliminated by successive washings with cold (4° C) ultrapure water until the supernatant appears colorless after centrifugation.

Drop casting method.[46] Inorganic helices (100 µg) were deposited on a 1 cm^2 quartz plate and allowed to dry under air. A porphyrin solution in DMF (7.5 µL, 5 mM) was deposited on top of the helices and left to air-dry in a 17 cm^3 closed box at 20°C.

Amine functionalization of silica helices. Inorganic helices were suspended in toluene at concentrations of 1g/L to 3 g/L, and 5 mL of the suspension was placed in a microwave tube. (3-aminopropyl) triethoxysilane (APTES) (40 µL, 0.17 mmol to 120 µL, 0.51 mmol) was added and the mixture was sonicated for at least 5 min. The tube was then placed in a microwave device (CEM Discovery 1.0) and heated for 4 h (100°C, 100W, ≈30 PSI). The unreacted APTES was then eliminated by successive centrifugation (12500 g, 30 min, 20° C) and sonication in ethanol.

Electrostatic grafting 1 mL of a 1 g.L-1 porphyrin solutions were mixed with a suspension of amine functionalized helices (1mL of a 1 g.L-1 suspension in ultra pure water). The resulting mixtures were stirred for 12 h. The unreacted porphyrins were then washed away via successive centrifugation (3893 g, 5 min, 20°C) and 5 min sonications in water.

Covalent grafting. 1 mL of a 1g/L hemin solution in anhydrous DMF was placed in a 5 mL round-bottom flask previously cleaned with piranha solution. 1-ethyl-3-[3-(dimethylamino)propyl]carbodiimide hydrochloride (EDC) (1mg, $5.1.10^{-3}$ mmol) and hydroxybenzotriazole (HOBT) (1 mg ($7.2.10^{-3}$ mmol) were added to the solution. The flask was covered and stirred under a nitrogen atmosphere in an ice bath for 1 h. Amine functionalized helices (1 mL of a 1 g/L suspension of in methanol) were added using a syringe. The resulting mixture was stirred, covered, for 48 h. The unreacted hemin was then washed away via successive centrifugations (3893 g, 5min, 20°C) and 5 min sonications in ethanol.

Materials and methods

Transmission electron microscopy (TEM) TEM observation was performed on a Philips EM 120 electron microscope operating at 120 kV, and the images were collected using a 2k × 2k Gatan ssCCD camera. Drop cast samples were prepared as the following. Inorganic helices (1 µg) suspended in ethanol were deposited on one carbon thin film copper TEM grid and left to dry. Then the adequate quantity of porphyrin solution in DMF (5 mM, 0.08 µL) was drop casted on top and also left to dry. For the hybrid samples, a pre-treatment of 30s air plasma irradiation of the carbon film is done in order to obtain an hydrophilic surface. Then the hybrid samples (1 µg) suspended in water were deposited and left to dry.

HR-TEM energy dispersive spectroscopy (EDS) The same TEM grids used previously for simple TEM observations were used for EDS mapping via TEM on a JEOL JEM 2200FS FEG HR 200 kV. The atomic percentage of the Fe (K) and silicon Si (K), in the different samples was estimated. For each sample several areas of the sample were studied and the average was calculated.

Fourier-transform infrared spectroscopy (FTIR) IR spectra were recorded with a Thermo-Nicolet Nexus 670 FTIR spectrometer, at a resolution of 4 cm^{-1}, by co-adding 50 scans. The suspended samples were directly deposited onto a CaF_2window and left to dry. All IR spectra were shown with air absorption subtracted out.

Electronic circular dichroism (ECD) ICD single scan spectra were recorded on a Jasco J-815 CD spectrometer. The scan rate was 200 $nm.min^{-1}$. All CD experiments were carried out with a 1cm^2 quartz plate at 20 °C. It should be mentioned that solid state chiral optical spectroscopy is sensitive to linear dichroism adulteration (LD). LD was measured for all dried samples and proved to be absent.

Magnetic circular dichroism (MCD) MCD spectra were obtained in the same spectrometer and conditions with which CD spectra were measured. In order to measure MCD signals, a permanent magnet PMCD-586 of 1.6 T from Jasco was added to the set-up. Both parallel and anti-parallel measurements were obtained by doing one measurement with one orientation of the permanent magnet and the other one with the other orientation, after turning it by 180° in the spectrometer. The same quartz plate orientation was kept during each analysis (EDC & MCD) to avoid linear dichroism effect even though it was negligible.

Magneto-chiral dichroism (MChD) MChD spectra were recorded with a locally built multichannel MChD spectrometer operating in the visible and near-infrared spectral window (420 to 1600 nm) between 4.0 and 300 K with an alternating magnetic field up to 2.0 T. A detailed description of the measurement apparatus has been reported elsewhere.[56] MChD measurements were performed on drop casted samples on quartz plates as described previously for ECD by adjusting the deposited quantities of helices and porphyrins. Thus, 48 µg of inorganic helices were deposited followed by the addition of 3.6 µL of 5 mM porphyrin solution on a 0.6x 0.8 cm^2 quartz plate.

Ultraviolet-visible spectroscopy (UV-vis) UV-vis spectroscopy was carried-out directly in the CD spectrometer. The porphyrin solutions were measured at 20°C in a 2mm width cell with a concentration between 0,060 mM and 0,025 mM for the TPPS based molecules and 0,150 mM for the Hemin. The drop casted samples have been analysed in the same conditions as CD measurements.

Author Contributions

Conceptualization: E.A. H., E.P.; Funding acquisition: E.A.H., E.P., G.L.J.A.R, C.T; Investigation: G.D., L.R., P.L., E.D., M.D.S.L.M., M.S.R., E.P., A.S., S.B., T.B., M.A.; Validation: S.B., T.B., M.A.; Project administration: E.A. H., E.P.; Supervision: E.A. H., E.P.; Visualization: G.D., E.A.H., E.P.; Writing original draft: E.A. H., E.P.; Writing Review: S.B., T.B., M.A., S.N., R.O., C.T., G.L.J.A.R., P.R.

Conflicts of interest

There are no conflicts to declare.

Acknowledgements

The authors acknowledge the ANR MaChiNaCo (PCR ANR-19-CE09-0018) for financial support. We thank Placamat platform for HRTEM measurements and IECB Chirality platform for CD measurements.

Notes and references

1 B. Bosnich, J. Am. Chem. Soc., 1966, 88, 2606–2606.

2 S. F. Mason, Chem. Phys. Lett., 1975, 32, 201–203.

3 S. Allenmark, Chirality, 2003, 15, 409–422.

4 M. Otagiri, K. Ikeda, K. Uekama, O. Ito and M. Hatano, Chem. Lett., 1974, 3, 679–682.

5 S. Takenaka, N. Matsuura and N. Tokura, Tetrahedron Lett., 1974, 15, 2325–2328.

6 Y. Li, X. Caumes, M. Raynal and L. Bouteiller, Chem. Commun., 2019, 55, 2162–2165.

7 T. Goto, Y. Okazaki, M. Ueki, Y. Kuwahara, M. Takafuji, R. Oda and H. Ihara, Angew. Chem. Int. Ed., 2017, 56, 2989–2993.

8 C. Song, M. G. Blaber, G. Zhao, P. Zhang, H. C. Fry, G. C. Schatz and N. L. Rosi, Nano Lett., 2013, 13, 3256–3261.

9 A. Kuzyk, R. Schreiber, Z. Fan, G. Pardatscher, E.-M. Roller, A. Högele, F. C. Simmel, A. O. Govorov and T. Liedl, Nature, 2012, 483, 311–314.

10 K. Maeda, D. Hirose, N. Okoshi, K. Shimomura, Y. Wada, T. Ikai, S. Kanoh and E. Yashima, J. Am. Chem. Soc., 2018, 140, 3270–3276.

11 G. L. J. A. Rikken and E. Raupach, Nature, 1997, 390, 493–494.

12 G. L. J. A. Rikken and E. Raupach, Nature, 2000, 405, 932–935.

13 Y. Kitagawa, H. Segawa and K. Ishii, Angew. Chem. Int. Ed., 2011, 50, 9133–9136.

14 M. Atzori, G. L. J. A. Rikken and C. Train, Chem. Eur. J., 2020, 26, 9784–9791.

15 M. Atzori, C. Train, E. A. Hillard, N. Avarvari and G. L. J. A. Rikken, Chirality, 2021, 33, 844–857.

16 M. Atzori, F. Santanni, I. Breslavetz, K. Paillot, A. Caneschi, G. L. J. A. Rikken, R. Sessoli and C. Train, J. Am. Chem. Soc., 2020, 142, 13908–13916.

17 M. Atzori, H. D. Ludowieg, Á. Valentín-Pérez, M. Cortijo, I. Breslavetz, K. Paillot, P. Rosa, C. Train, J. Autschbach, E. A. Hillard and G. L. J. A. Rikken, Sci. Adv., 2021, 7, eabg2859.

18 M. Atzori, K. Dhbaibi, H. Douib, M. Grasser, V. Dorcet, I. Breslavetz, K. Paillot, O. Cador, G. L. J. A. Rikken, B. Le Guennic, J. Crassous, F. Pointillart and C. Train, J. Am. Chem. Soc., 2021, 143, 2671–2675.

19 K. Dhbaibi, M. Grasser, H. Douib, V. Dorcet, O. Cador, N. Vanthuyne, F. Riobé, O. Maury, S. Guy, A. Bensalah-Ledoux, B. Baguenard, G. L. J. A. Rikken, C. Train, B. Le Guennic, M. Atzori, F. Pointillart and J. Crassous, Angewandte Chemie International Edition, 2023, 62, e202215558.

20 N. B. Baranova and B. Y. Zel'Dovich, Mol. Phys., 1979, 38, 1085–1098.

21 C. Train, M. Gruselle and M. Verdaguer, Chem. Soc. Rev., 2011, 40, 3297.

22 X. Wang, S.-Q. Wang, J.-N. Chen, J.-H. Jia, C. Wang, K. Paillot, I. Breslavetz, L.-S. Long, L. Zheng, G. L. J. A. Rikken, C. Train, X.-J. Kong and M. Atzori, J. Am. Chem. Soc., 2022, 144, 8837–8847.

23 R. Giovannetti, in Macro To Nano Spectroscopy, ed. J. Uddin, InTech, 2012.

24 N. C. Maiti, S. Mazumdar and N. Periasamy, J. Phys. Chem. B, 1998, 102, 1528–1538.

25 J. Sobczyński, H. H. Tønnesen and S. Kristensen, Pharmazie, 2013, 68, 2, 100–109.

26 S. Okada and H. Segawa, J. Am. Chem. Soc., 2003, 125, 2792–2796.

27 K. Ishii, S. Hattori and Y. Kitagawa, Photochem. Photobio. Sci., 2020, 19, 8–19.

28 H. Watarai and Y. Kurahashi, Anal. Chem., 2016, 88, 4619–4623.

29 L. Zhang, T. Wang, J. Jiang and M. Liu, Aggregate, 2023, 4, e198.

30 R. Oda, I. Huc, M. Schmutz, S. J. Candau and F. C. MacKintosh, Nature, 1999, 399, 566–569.

31 Y. Okazaki, T. Buffeteau, E. Siurdyban, D. Talaga, N. Ryu, R. Yagi, E. Pouget, M. Takafuji, H. Ihara and R. Oda, Nano Lett., 2016, 16, 6411–6415.

32 Y. Okazaki, J. Cheng, D. Dedovets, G. Kemper, M.-H. Delville, M.-C. Durrieu, H. Ihara, M. Takafuji, E. Pouget and R. Oda, ACS Nano, 2014, 8, 6863–6872.

33 K. Sugiyasu, S. Tamaru, M. Takeuchi, D. Berthier, I. Huc, R. Oda and S. Shinkai, Chem. Commun., 2002, 1212–1213.

34 T. Delclos, C. Aimé, E. Pouget, A. Brizard, I. Huc, M.-H. Delville and R. Oda, Nano Lett., 2008, 8, 1929–1935.

35 N. Ryu, Y. Okazaki, K. Hirai, M. Takafuji, S. Nagaoka, E. Pouget, H. Ihara and R. Oda, Chem. Commun., 2016, 52, 5800–5803.

36 M. Attoui, E. Pouget, R. Oda, D. Talaga, G. Le Bourdon, T. Buffeteau and S. Nlate, Chem. Eur. J., 2018, 24, 11344–11353.

37 Z. Cao, A. Scalabre, S. Nlate, S. Buffière, R. Oda, E. Pouget and B. Bibal, Chem. Eur. J., 2021, 27, 427–433.

38 Y. Okazaki, N. Ryu, T. Buffeteau, S. Pathan, S. Nagaoka, E. Pouget, S. Nlate, H. Ihara and R. Oda, Chem. Commun., 2018, 54, 10244–10247.

39 J. Cheng, G. Le Saux, J. Gao, T. Buffeteau, Y. Battie, P. Barois, V. Ponsinet, M.-H. Delville, O. Ersen, E. Pouget and R. Oda, ACS Nano, 2017, 11, 3806–3818.

40 Y. Negrín-Montecelo, A. Movsesyan, J. Gao, S. Burger, Z. M. Wang, S. Nlate, E. Pouget, R. Oda, M. Comesaña-Hermo, A. O. Govorov and M. A. Correa-Duarte, J. Am. Chem. Soc., 2022, 144, 1663–1671.

41 P. Liu, W. Chen, Y. Okazaki, Y. Battie, L. Brocard, M. Decossas, E. Pouget, P. Müller-Buschbaum, B. Kauffmann, S. Pathan, T. Sagawa and R. Oda, Nano Lett., 2020, 20, 8453–8460.

42 R. Oda, F. Artzner, M. Laguerre and I. Huc, J. Am. Chem. Soc., 2008, 130, 14705–14712.

43 A. Scalabre, Y. Okazaki, B. Kuppan, T. Buffeteau, F. Caroleo, G. Magna, D. Monti, R. Paolesse, M. Stefanelli, S. Nlate, E. Pouget, H. Ihara, D. M. Bassani and R. Oda, Chirality, 2021, 33, 494–505.

44 R. Nag, Y. Okazaki, A. Scalabre, Z. Anfar, S. Nlate, T. Buffeteau, R. Oda and E. Pouget, Chem. Commun., 2022, 58, 13515–13518.

45 A. Brizard, D. Berthier, C. Aimé, T. Buffeteau, D. Cavagnat, L. Ducasse, I. Huc and R. Oda, Chirality, 2009, 21, E153–E162.

46 P. Liu, Y. Battie, T. Kimura, Y. Okazaki, P. Pranee, H. Wang, E. Pouget, S. Nlate, T. Sagawa and R. Oda, Nano Lett., 2023, 23, 3174–3180.

47 J. Gao, W. Wu, V. Lemaire, A. Carvalho, S. Nlate, T. Buffeteau, R. Oda, Y. Battie, M. Pauly and E. Pouget, ACS Nano, 2020, 14, 4111–4121.

48 P. Liu, Y. Battie, Y. Okazaki, N. Ryu, E. Pouget, S. Nlate, T. Sagawa and R. Oda, Chem. Commun., 2021, 57, 12024–12027.

49 C. Oliveras-González, F. Di Meo, A. González-Campo, D. Beljonne, P. Norman, M. Simón-Sorbed, M. Linares and D. B. Amabilino, J. Am. Chem. Soc., 2015, 137, 15795–15808.

50 M. Stefanelli, M. Savioli, F. Zurlo, G. Magna, S. Belviso, G. Marsico, S. Superchi, M. Venanzi, C. Di Natale, R. Paolesse and D. Monti, Frontiers in Chemistry.

51 L. Zhao, A. Li, R. Xiang, L. Shen and L. Shi, Langmuir, 2013, 29, 8936–8943.

52 F. Würthner, T. E. Kaiser and C. R. Saha-Möller, Angewandte Chemie International Edition, 2011, 50, 3376–3410.

53 O. Ohno, Y. Kaizu and H. Kobayashi, The Journal of Chemical Physics, 1993, 99, 4128–4139.

54 G. Socrates, Infrared and Raman Characteristic Group Frequencies: Tables and Charts, 3rd Edition, Wiley, 3rd edn., 2004.

55 G. Petrucci, A. Gabbani, I. Faniayeu, E. Pedrueza-Villalmanzo, G. Cucinotta, M. Atzori, A. Dmitriev and F. Pineider, Appl. Phys. Lett., 2021, 118, 251108.

56 G. Kopnov and G. L. J. A. Rikken, Rev. Sci. Inst., 2014, 85, 053106.